Review of Scientific Instruments

RESEARCH ARTICLE | JUNE 09 2023

A mid-infrared laser microscope for the time-resolved study of light-induced protein conformational changes

Maria Eleonora Temperini ; Raffaella Polito ; Antonia Intze ; Raymond Gillibert ; Fritz Berkmann ; Leonetta Baldassarre ; Valeria Giliberti ; Michele Ortolani

Check for updates

Rev. Sci. Instrum. 94, 064102 (2023)
https://doi.org/10.1063/5.0136676

View Online
Export Citation

26 February 2025 15:44:32

AIP Publishing

A mid-infrared laser microscope for the time-resolved study of light-induced protein conformational changes

Cite as: Rev. Sci. Instrum. 94, 064102 (2023); doi: 10.1063/5.0136676
Submitted: 28 November 2022 • Accepted: 26 May 2023 •
Published Online: 9 June 2023

View Online Export Citation CrossMark

Maria Eleonora Temperini,[1,2] Raffaella Polito,[1] Antonia Intze,[1,2] Raymond Gillibert,[1] Fritz Berkmann,[1] Leonetta Baldassarre,[1] Valeria Giliberti,[2] and Michele Ortolani[1,2,a)]

AFFILIATIONS

[1] Department of Physics, Sapienza University of Rome, Piazzale Aldo Moro 2, Rome 00185, Italy
[2] Center for Life Nano & Neuro Science CL2NS, Istituto Italiano di Tecnologia, Viale Regina Elena 291, Rome 00161, Italy

[a)] **Author to whom correspondence should be addressed:** michele.ortolani@roma1.infn.it

ABSTRACT

We have developed a confocal laser microscope operating in the mid-infrared range for the study of light-sensitive proteins, such as rhodopsins. The microscope features a co-aligned infrared and visible illumination path for the selective excitation and probing of proteins located in the IR focus only. An external-cavity tunable quantum cascade laser provides a wavelength tuning range (5.80–6.35 μm or 1570–1724 cm^{-1}) suitable for studying protein conformational changes as a function of time delay after visible light excitation with a pulsed LED. Using cryogen-free detectors, the relative changes in the infrared absorption of rhodopsin thin films around 10^{-4} have been observed with a time resolution down to 30 ms. The measured full-width at half maximum of the Airy disk at $\lambda = 6.08$ μm in transmission mode with a confocal arrangement of apertures is 6.6 μm or 1.1λ. Dark-adapted sample replacement at the beginning of each photocycle is then enabled by exchanging the illuminated thin-film location with the microscope mapping stage synchronized to data acquisition and LED excitation and by averaging hundreds of time traces acquired in different nearby locations within a homogeneous film area. We demonstrate that this instrument provides crucial advantages for time-resolved IR studies of rhodopsin thin films with a slow photocycle. Time-resolved studies of inhomogeneous samples may also be possible with the presented instrument.

© 2023 Author(s). All article content, except where otherwise noted, is licensed under a Creative Commons Attribution (CC BY) license (http://creativecommons.org/licenses/by/4.0/). https://doi.org/10.1063/5.0136676

26 February 2025 15:44:32

I. INTRODUCTION

Changes in the protein conformation under a given external stimulus constitute the basic mechanism of many protein functions. Vibrational spectroscopy in the mid-infrared (mid-IR) range can track these slight modifications of the protein structure in a label-free fashion and in a quasi-physiologic environment.[1,2] In particular, in the IR wavelength range from 5.5 to 6.5 μm (~1500–1700 cm^{-1}), the amide-I and amide-II bands are observed, whose detailed line shape is sensitive to the angle and length of each peptide bond, which allows for the identification of secondary structures.[3] Rhodopsins are cell-membrane proteins undergoing light-induced conformational changes due to the retinal, a non-proteic cofactor that absorbs visible light and transfers it to the protein, partly in the form of vibrational energy. Visible light absorption is exploited by living cells expressing rhodopsins for energy harvesting or signal transduction,[4] thereby triggering applications in organic photovoltaics,[5] active matter control,[6] and optogenetics.[7] Under visible light illumination, the retinal undergoes photoisomerization that can be tracked through the C=C vibration, also falling in the above-mentioned IR range around 1510–1580 cm^{-1}. These protein/retinal structure changes are reversible (the initial dark-adapted state is eventually recovered by the illuminated proteins), and therefore, the sequence of conformational changes, connecting transient intermediate states, is named the rhodopsin photocycle, with time scales ranging from femtoseconds to fractions of a second,[4] with longer time scales being of higher biological interest.[8,9]

Fourier transform IR (FTIR) difference spectroscopy is the standard approach to monitoring the molecular mechanisms underlying the photocycle of rhodopsins, usually performed with time-resolved spectroscopy (TRS) modules.[10] TRS-FTIR of biomolecules, however, generally suffers from a low signal to noise ratio (SNR) of

© Author(s) 2023

10^3 that prevents one from following, in the time domain, the small mid-IR relative absorption differences, of the order of 10^{-3}–10^{-4}, taking place during a single photocycle: averaging over many tens of repeated photocycles is then required to increase the SNR.[8] In TRS, the time between subsequent photocycles should obviously be longer than the return time of the given protein to the dark-adapted state. This return time depends on environmental conditions and ranges from a few tens of milliseconds, as for, e.g., the wild-type bacteriorhodopsin (BR),[11] to many minutes, as for some slow mutants of Channelrhodopsin (ChR).[9]

In the case of TRS-FTIR measurements, this translates to a total experimental time of several hours or even days. In addition, the final state of the photocycle may be slightly different from the initial dark-adapted state. Sample replacement within the same homogeneous dark-adapted sample volume at each photocycle start is then the best possible approach to ensuring the consistency of the data to be averaged. For proteins in liquid solutions, sample replacement can be achieved with a peristaltic pump.[12] However, this configuration is particularly cumbersome for IR transmission spectroscopy due to the strong absorption of water in the IR. For dry cell-membrane films deposited on flat solid supports, which have provided mid-IR results compatible with those collected in liquid solutions with the advantage of water-free sample handling,[13,14] a sample replacement technique has not been reported yet.

In this work, we build an instrument that replaces the sample portion in the IR probing volume, featuring only dark-adapted proteins, also in dry films. We do this by precisely displacing on the film surface, at each photocycle start, a small focal spot consisting of a spatially coincident visible excitation beam and a mid-IR laser probe beam, as they are both focused with the same achromatic reflective objective. To this aim, it was necessary to build a custom confocal microscope because the use of tunable mid-IR lasers in micro-spectroscopy is rather recent: the existing commercial systems have either been designed for fast imaging in widefield mode or have been optimized for acquisition speed using laser-scanning technology.[15–17] As far as we know, this is the first mid-IR laser confocal microscope optimized for TRS: starting from few-μl droplets of the sample, we are able to monitor even the slow molecular mechanisms underlying the photocycle of rhodopsins in a short total experimental time of a few minutes, to be contrasted with the days-long experiments required with single-point FTIR-TRS spectrometers, where one has to wait for large sample area dark adaptation before each photocycle starts.

The schematic of the custom microscope is shown in Fig. 1. The quantum cascade laser (QCL) beam, tuned at the specified mid-IR wavelength for protein structural change detection, is co-aligned with a pulsed light-emitting diode (LED) beam, with color and pulse structure suitable for specific protein excitation. A He–Ne laser with approximately the same beam diameter as the QCL serves for microscope alignment with a visible camera. The co-aligned beams are sent to a Cassegrain objective for reflection mode (or to an objective pair for transmission mode), and the reflected/transmitted beam is detected with a cryogen-free mercury–cadmium–telluride (MCT) photodiode and sent to a lock-in amplifier with the reference frequency set at the repetition rate of the QCL. A master oscillator is used to synchronize the LED pulse, the XY stage movement for sample replacement, and the data acquisition from the lock-in amplifier. For an initial demonstration with our microscope, we have chosen the photoactive protein bacteriorhodopsin (BR) in two different variants: the wild-type BR featuring a fast return time of less than 30 ms[10] and the BR D96N mutant (hereafter called the "slow mutant") featuring a long return time of many seconds.[18]

II. MICROSCOPE DESCRIPTION

A. Signal detection and data acquisition

Figure 1(a) presents the schematic of the microscope. The QCL is an external cavity-tunable QCL (ECqcL™) (DRS Daylight Solutions, model no. 41060, presently named "Hedgehog™"), with a

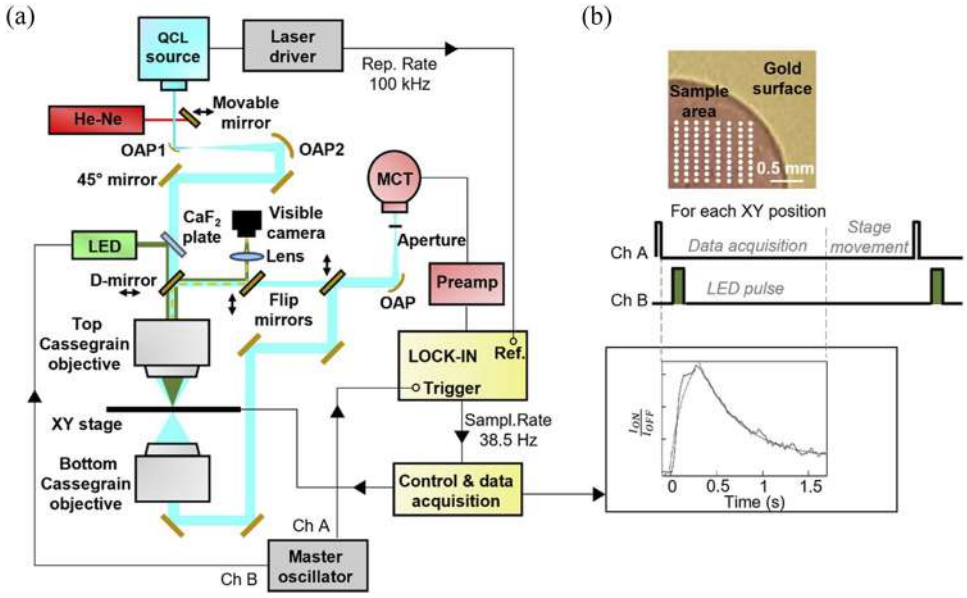

FIG. 1. (a) Schematic illustration of the QCL-microscope highlighting the principal optical elements and the hardware components for instrument control and data acquisition. (b) Example of an experimental routine for the time-trace acquisition on a BR film with sample replacement at each photocycle. The XY mapping step chosen for dark-adapted sample replacement is 250 μm, and the number of steps is 80, corresponding to different locations on the sample drop.

26 February 2025 15:44:32

© Author(s) 2023

tuning range of 5.80–6.35 μm and a peak output power of <300 mW. Although it can work in continuous wave mode, we choose to operate it in pulsed mode at a 100 kHz repetition rate and 0.6% duty cycle (60 ns pulse duration), eliminating the need for liquid cooling of the laser hutch. The IR radiation reflected or transmitted by the sample is detected pixel-by-pixel with a cryogen-free thermoelectric-cooled MCT detector (Infrared Associates, Inc., model no. MCT-9-TE-1.00). The wavelength sensitivity of the detector is 11–5 μm, the response time is below 1 μs, and the preamplifier bandwidth is 1 MHz. The use of a fast detector makes it possible to work with the repetition rate of the QCL (100 kHz) as the reference of a lock-in amplifier (Stanford Research Corp., model no. SR830), allowing us to use very short laser pulses (60 ns), for which external cooling of the mid-IR source is not necessary and sample heating is reduced to minimum. The preamplifier output is sent to the lock-in amplifier whose integration time is set either to 30 or to 100 ms depending on signal intensity, and the output sampling rate is set to 38.5 Hz, which gives us a SNR of 10^3 per each data point. To obtain a SNR of 10^4, we must average over 10^2 photocycles. A master oscillator (Quantum Composer, Inc., model no. 9420) triggers the data acquisition from the lock-in amplifier with a PC and drives the LED pulses, thanks to a specific current driver (Thorlabs, model no. DC2200). In this work, we set the duration of the LED pulses between 10 ms and 2 s and the rise time at 0.1 ms. The data acquisition software written in Python on the PC moves the piezo-driven XY stage (Physik Instrumente, model no. PI M-687.UO) by pre-defined X and Y steps [250 μm in the example of Fig. 1(b)] after each time trace acquisition from the lock-in amplifier [typically 100 data points at 38.5 Hz, i.e., ~2 s as in the example of Fig. 1(b)].

B. Optical paths

In Fig. 2, we show the images of the microscope taken from the three viewing angles indicated in the schematic drawing of

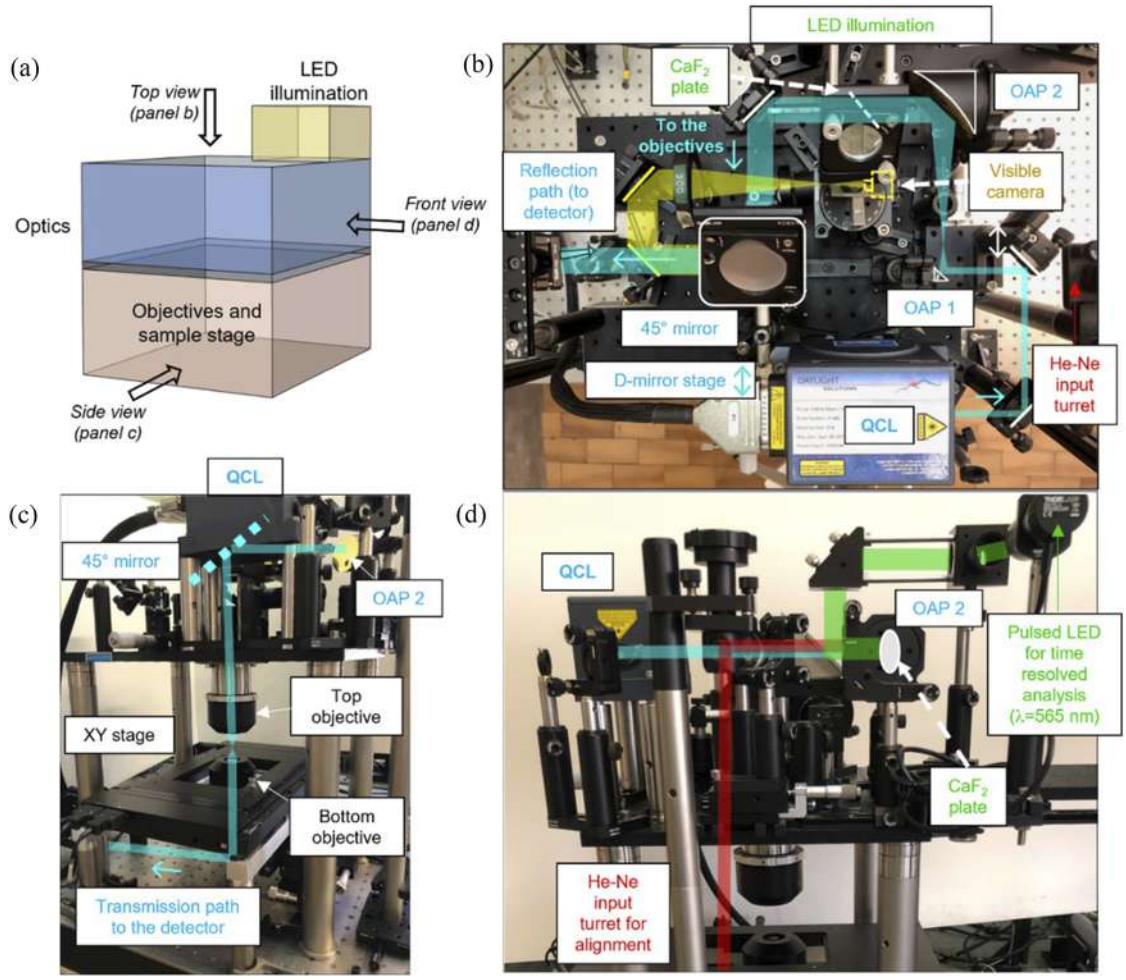

FIG. 2. (a) Schematic representation of the three main sections of the microscope and pictures of (b) the top view, (c) the side view, and (d) the front view. The different optical paths are represented with different colors: QCL beam in light blue, visible CMOS camera path in yellow, alignment He–Ne beam in red, and exciting LED beam in green.

26 February 2025 15:44:32

© Author(s) 2023

Fig. 2(a), with the different optical paths highlighted in different colors. The mid-IR path (light blue color) starts from the QCL output port with a 3 mm diameter parallel beam (the M^2 factor provided by the manufacturer is 1.2 and <5 mrad of beam divergence) [Fig. 2(b)]. A Gaussian beam expander made by two 90° off-axis parabolic mirrors (OAP1 and OAP2), with focal lengths of 25 and 100 mm, respectively, expands the QCL beam diameter to 12 mm, a value that matches the entrance aperture diameter of the infinity corrected Cassegrain microscope objectives with NA = 0.4 (Beck Optronic Solutions, model no. 5002), visible in Fig. 2(c). A He–Ne laser (Melles Griot, model no. 05-LHP-911) emitting in the red with a beam diameter of 3 mm is co-aligned with the QCL beam through an input turret [see the red color beam in Fig. 2(d)]. It is used for the alignment of the beam expander, of the objectives, and of the sample focal plane, also exploiting a visible CMOS camera installed in the reflection path [Thorlabs, model no. DCU224C, yellow color beam in Fig. 2(b)].

In Fig. 2(c), we show the sample stage with the two objectives mounted along a vertical optical axis, defined through a large 45° plane mirror (50 mm diameter) with easy-to-access alignment knobs. The MCT detector is installed on the optical table and reached with a second 45° mirror followed by a last adjustable parabolic mirror (not visible in the pictures in Fig. 2). For operation in reflection mode, a D-shaped half mirror is positioned by a manual stage after the 45° mirror and above the illumination objective. The output mid-IR beam reflected by the D-mirror is sent down to the optical table to the same detector [see Fig. 2(b)] by displacing the flip-mirror previously used for alignment with the CMOS camera. For operation in transmission mode, a second identical Cassegrain objective positioned below the XY piezo-stage is precisely co-aligned to ensure confocality using the He–Ne beam and a second CMOS camera. The objectives feature a large working distance of 20 mm useful for complicated sample mounts (microfluidics, cryogenics, etc.). The total free space between the objectives in transmission mode is 40 mm.

The relevant feature of our microscope for the time-resolved study of proteins, however, is the use of the same illumination objective for both the mid-IR probe and the visible illumination channel [green color beam in Fig. 2(d)], which reduces the illuminated area on the protein film and keeps the rest of the protein sample in dark-adapted conditions until it is probed by the microscope beams. The aluminum-coated reflective objectives provide a fully achromatic focusing behavior in the mid-IR and visible ranges, allowing one to choose the illumination wavelength in the entire LED availability range from violet to near-IR (Thorlabs MxxxLx series, output power around 250 mW), according to the specific protein under study.[19] Multi-color illumination can also be implemented with dichroic filters mounted in a filter box. The LED illumination is passed into a lens telescope equipped with an iris pupil that produces an approximately collimated beam of 10 mm diameter and sent to a 1 mm thick CaF_2 plate that works as a dichroic beam combiner for mid-IR and LED beams [see Figs. 2(b) and 2(d)]. The CaF_2 plate transmits 96% of the mid-IR power and reflects 4% of the visible illumination power, i.e., around 10 mW. Note that in reflection mode, the LED illumination power is halved by the presence of the D-mirror just like the IR probe power, but the LED current can be adjusted to provide double illumination power. The co-aligned beams from the LED and the QCL are focused by the Cassegrain objective onto the sample surface. The collimation of the LED lens telescope is adjusted to make the LED and mid-IR foci perfectly overlap on the sample surface. For our median QCL wavelength of $\lambda = 6.08\ \mu m$ and almost ideal QCL M^2 factor of 1.2, we can expect the mid-IR spot size in transmission mode to be an Airy disk with diameter $D = 1.22\lambda/NA = 18.5\ \mu m$ given by diffraction theory. The theoretical lateral resolution limit estimated as the full width at half maximum (FWHM) of the Airy disk obtained with the Abbe formula is $\Delta x = 0.5\lambda/NA = 7.6\ \mu m$.

III. MICROSCOPE CHARACTERIZATION

A. Spatial resolution

Imaging in reflection mode of a cross-shaped lithographic pattern on a silicon substrate filled with evaporated gold and dielectric materials is demonstrated in Figs. 3(a) and 3(b). The chosen pixel size of 10 × 10 μm^2, comparable to the employed wavelength of 6.08 μm, evidences the good imaging and material contrast capabilities of our microscope: different materials provide different reflectance values, although the feature size is sometimes smaller than the wavelength. One can note that the spatial resolution along the *y*-direction is lower than that along the *x*-direction. This asymmetric behavior is due to the elongated spot size of the IR

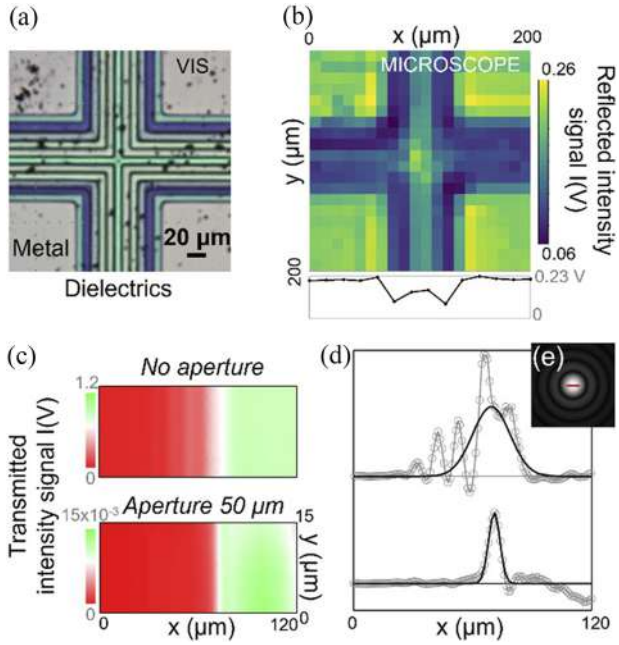

FIG. 3. (a) Visible image of a lithographic target employed for the spatial resolution test and (b) mid-IR image in reflection mode with a D-mirror at $\lambda = 6.08\ \mu m$ of the same target. The pixel size is 10 × 10 μm^2. The different resolution in the *x* and *y* directions is due to the use of a D-mirror.[20] (c) Experimental maps of a gold/silicon lithographic edge acquired in transmission mode without an aperture (top) and with a 50 μm aperture at the detector position (bottom). The step size is 1 μm. (d) Numerical differentiation of the data in (c) averaged along the *y*-direction (dotted gray curves) and Gaussian fitting curve (black curve). (e) Image of the Airy disk in which the dimension of the FWHM used for the lateral resolution estimation is highlighted (red line).

26 February 2025 15:44:32

© Author(s) 2023

beam caused by the presence of the D mirror in the reflectance measurements.[20]

To quantitatively evaluate the laser spot size in the focal plane and demonstrate the confocality of our microscope, IR transmission maps were taken across the edge of a fully gold-coated patch defined by electron-beam lithography (edge sharpness <100 nm) on a silicon wafer. They are reported in Figs. 3(c) and 3(d), acquired, respectively, without any aperture and with an aperture of 50 μm in the focal plane of the detector. The maps have a 120 × 15 μm^2 dimension and a step-size of 1 μm. To compare the lateral resolution of the microscope in the two configurations, we averaged the signal acquired along the x-direction over the 15 rows to increase the signal-to-noise ratio. We then calculated the first derivative of the x-scan signal [dotted gray curves in Fig. 3(d)], and we did a Gaussian fit [black curve in Fig. 3(d)]. The lateral resolution was thus estimated as the FWHM of the Gaussian fit, obtaining a value of 22 μm in the absence of any aperture and an improved value of 6.6 μm (~1.1λ) by adding the 50 μm aperture at the detector position. Figure 3(e) represents the theoretical intensity pattern due to diffraction from a circular aperture (Airy disk and rings), where we approximately indicate with a red arrow the definition of "lateral resolution" used throughout this paper, i.e., the FWHM of the central disk estimated from a Gaussian fit. The experimental value of 6.6 μm compares well with the Abbe formula calculation (7.6 μm), with the small discrepancy probably due to the exclusion of the negative feature at x = 75 μm in Fig. 3(d) from the fitting range.

We specify that for the time-resolved experiments on light-sensitive proteins, which are reported below, the measurements are performed in reflection mode without the use of any aperture at the detector position. The reason is that, in this kind of experiments, we are not interested in a high lateral resolution but rather in a high sensitivity to relative intensity changes of the order of 10^{-4} so that it is important to maximize the signal. In this configuration, the lateral resolution is comparable to the one obtained in transmission mode (i.e., ~20 μm) and the IR spot size of around 32 μm (defined as the diameter of the Airy disk) limits the minimum lateral movement of the XY piezo-stage applied after each LED pulse illumination to replace the previously illuminated portion of the sample with a dark-adapted portion. The divergence angle of the LED beam is adjusted with a collimator to produce a diameter of the LED spot on the sample plane corresponding to the IR focal spot size of 32 μm. In a typical thin film with a diameter of 1 mm, obtained by drop-casting of a protein solution, such a small IR spot diameter accounts for a number of possible dark-adapted sample replacements of the order of 10^3, given by the ratio between the film area and the spot area. This simple calculation clarifies the advantage of using a microscope to perform time-resolved IR analysis of rhodopsins in a short time frame, even if not in a confocal configuration.

We note that the present sample can be considered very homogeneous from the point of view of time-dependent response; however, this microscope could well be suited for studying more complex systems that may feature an inhomogeneous time-dependent behavior.

B. Time-resolved experiment on light-sensitive proteins

For the demonstration of the time-resolved IR study of light-induced protein conformational changes with our microscope, we chose a thick film of the protein BR on a gold substrate; therefore, we used the reflection mode. A BR film was produced by drop-casting 10 μl of purple membrane suspension on an ultra-flat gold surface [Fig. 4(a)], obtaining a total dried-drop area of around 4 mm^2. The purple membrane of *Halobacterium salinarum* [see Fig. 4(b) for a typical topography measured with an atomic force microscope (AFM)] contains almost exclusively BR;[21] therefore, we can identify the measured IR absorbance with the protein absorbance, neglecting reflection losses (the lipidic component is transparent around λ = 6 μm). The film thickness is inhomogeneous, and it varies between 1 and 3 μm depending on the position and it contains a high number of disconnected purple membrane flakes. The IR reflection map of a small section of the drop boundary taken with our microscope is shown in Fig. 4(c). The drop edge and the reflection variations inside the drop are clearly resolved at the pixel level (the chosen pixel size was 10 × 10 μm^2), as expected. The reflected signal is very low at the center of the film as the film thickness is close to half the absorption length of the amide-I band of proteins. The small blue spots outside the drop boundary correspond to sparse ensembles of single membrane flakes, sometimes stacked as double or triple layers, as confirmed by AFM imaging [Fig. 4(b) was taken approximately in the location marked with the number "4" in Fig. 4(c)].[22] In Fig. 4(d), we show line-scans at the

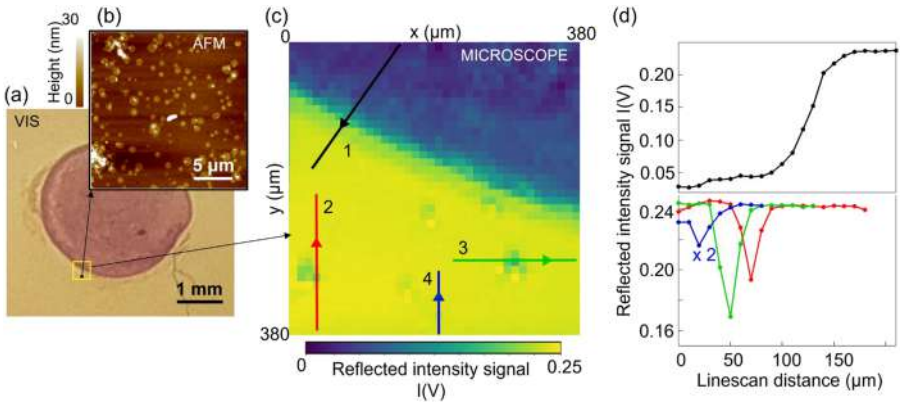

FIG. 4. (a) Picture of a dried drop of BR. (b) AFM image of a representative area outside the dried drop, showing the sparse assembly of individual purple membrane patches (thickness of 5 nm). (c) Mid-IR reflectance map at λ = 6.01 μm of one edge of the drop of panel (a): the low intensity pixels (blue) indicate BR rich areas inside the drop, and the high intensity pixels (yellow) indicate the gold substrate, where sparse membrane assemblies appear in green. (d) Four line-scans extracted from the map in (c) indicated by arrows with the same color code therein.

26 February 2025 15:44:32

© Author(s) 2023

edge of the film ("1") and across membrane ensembles outside the film. Interestingly, the single-membrane ensembles marked with "2, 3, and 4" could be clearly detected with our microscope; however, AFM-assisted IR nanospectroscopies remain the clear choice for single-membrane IR spectroscopy.[14,23] In this context, the present microscope will serve as a far-field benchmark for forthcoming AFM-IR time-resolved spectroscopy data.

We first study a film made of the wild-type BR protein to precisely determine the sign and the amplitude of the absorption change at specific mid-IR wavelengths. Figure 5(a) shows a benchmark FTIR difference-spectrum acquired under protein steady-state conditions: I_{OFF} and I_{ON} represent, respectively, the reflected intensity taken in the dark and under continuous visible illumination. Four significant mid-IR wavelengths selected for the QCL-microscope experiment have been highlighted: $\lambda_1 = 6.08\ \mu$m ($\omega_1 = 1/\lambda_1 = 1644\ cm^{-1}$) close to the center of the amide-I band and with minimum atmospheric attenuation, where the alpha-helix absorption has a maximum; $\lambda_2 = 6.19\ \mu$m ($\omega_2 = 1/\lambda_2 = 1616\ cm^{-1}$) at the tail of the amide-I band; $\lambda_3 = 6.29\ \mu$m ($\omega_3 = 1/\lambda_3 = 1590\ cm^{-1}$) within the amide-II band; and $\lambda_4 = 6.35\ \mu$m ($\omega_4 = 1/\lambda_4 = 1575\ cm^{-1}$) close to the strongest retinal absorption change. In Fig. 5(b), we show the time-resolved traces obtained with our microscope at the four selected wavelengths (ω_{1-4}) employing an excitation LED with an emission wavelength $\lambda_{ex} = 565$ nm and a pulse duration of 60 ms. The lock-in integration time was 30 ms, corresponding to the output sampling rate. The time traces can be acquired at all mid-IR wavelengths within the entire tuning range of the QCL, potentially making our microscope a continuously tunable instrument; however, the SNR at wavelengths different from λ_1 is much lower, due to both low emitted power from the specific QCL employed and much higher atmospheric attenuation at λ different from $\lambda_1 = 6.08\ \mu$m. The use of time-resolved traces at a few discrete wavelengths to characterize changes in the vibrational spectrum is not uncommon: one can fairly assume that the signal at nearby wavelengths within the same spectral feature specific to a single vibrational band would follow the same time trace.[24]

We then studied a film made of the BR D96N "slow mutant" sample to demonstrate the sample replacement advantage of our microscope. The time traces taken at $\omega_1 = 1644\ cm^{-1}$ are shown in Fig. 5(c). If compared to the previous experiment on wild-type BR, a much longer LED pulse duration (1.5 s), longer lock-in integration time (300 ms), and lower output sampling rate (10 Hz) had to be employed because of the much lower density of active BR D96N proteins in the membranes if compared to the wild-type BR sample, probably due to a weaker retinal–protein bond in the mutant. The average of 80 photocycles repeated at a fixed position (i.e., without scanning the XY stage) is shown as a black curve, while the average of 80 photocycles measured in 80 different locations with our automated sample-replacement routine is shown as a red curve. One can immediately see that the two curves are different. The fixed-position time-trace [black curve in Fig. 5(c)] increases with a characteristic exponential time constant $\tau_{th} = 0.6$ s while the LED is turned on, and it decreases with a relaxation time constant indistinguishable from τ_{th} when the illumination is turned off. This indicates that, in the case of BR D96N without sample replacement, the measured conformational changes have a trivial photothermal origin, i.e., a local temperature increase due to the absorption of visible light power. In other words, after the first LED pulse has hit the proteins in their dark-adapted BR state, the subsequent 79 LED pulses hit

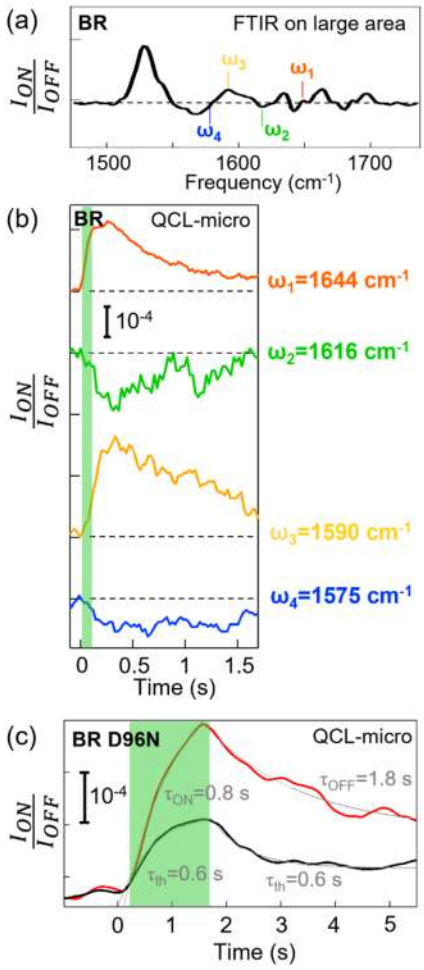

FIG. 5. (a) FTIR reference difference spectrum on a large area sample. (b) Time traces of the fast wild-type BR protein acquired with our QCL microscope at different laser wavelengths [note the sign of the spectral differences matching that of panel (a), same color code]. (c) Time traces of the slow mutant BR D96N acquired with our QCL microscope at $\omega_1 = 1644\ cm^{-1}$ without and with sample replacement (black and red curves, respectively).

the same proteins in a non-adapted state; therefore, the excess of photon energy causes the heating of both the proteins and water molecules, leading to variations in frequencies and widths of the vibrational bands.[25,26] Note that, instead, the sample heating and the damage from the QCL radiation are estimated to be negligible due to the low duty cycle employed in this experiment. The sample-replacement time-trace [red curve in Fig. 5(c)] shows two different characteristic exponential times for the two time intervals when the LED is turned on and off ($\tau_{ON} = 0.8$ s and $\tau_{OFF} = 1.8$ s). The time traces can be further analyzed to obtain the time scales of the slow-mutant photoactivity,[27] which were completely missed in the fixed-position experiment without sample replacement. We conclude that the correct procedure to measure the photocycle of the slow mutant, always starting from the dark-adapted BR state, is

26 February 2025 15:44:32

© Author(s) 2023

obviously the dark-adapted sample replacement, here achieved by XY mapping with our microscope.

IV. ULTIMATE TIME RESOLUTION AND ADVANTAGES

Protein photocycles span a large variety of characteristic timescales, from femtoseconds[28] (photo-isomerization and electronic transitions, in general) and picoseconds[29–31] (lifetime of vibrational modes) up to micro- and milliseconds (conformational changes and rearrangement of the retinal–protein complex) and return times of seconds to minutes.[4] The development of a single time-resolved IR spectrometer that can cover all these timescales has always proven to be extremely challenging. The millisecond timescale is probably the most relevant for transmembrane ion-pump proteins and for optogenetic gate proteins that can trigger signals in neurons, as this is ultimately the scale of observation of the behavior of neural systems *in vivo*.[32] In this work, we have referred to "time resolution" as the capability to resolve mid-IR absorption changes in the 10–5000 ms range in a single data acquisition event, a task that cannot be easily executed by present-day FTIR spectro meters with the rapid-scan option. The lock-in integration time set between 30 and 300 ms constitutes the lower boundary of the time resolution of the measurements presented in this work. Improvements in SNR, which can be obtained by replacing the QCL with a high-duty-cycle model, could provide the present microscope with time resolutions of at least 1 ms. The XY stage movement time is the present temporal bottleneck; therefore, a smaller focal spot diameter and, hence, smaller steps could help with increasing the number of averaged time traces in a given measurement time. Finally, the substitution of the lock-in amplifier with a fast data acquisition board for direct time-resolved trace acquisition from a fast (photoconductive) MCT detector could lead to an ultimate time resolution of a few tens of nanoseconds[33] with no changes to the optical setup, apart from nanosecond-pulsed visible lasers instead of LEDs for illumination. This latter instrumental improvement would allow one to investigate the initial fast steps of slow photocycle proteins, such as most of the ChR variants and the BR slow mutants.[34]

Comparing our QCL microscope with other available IR setups, the high power spectral density of the IR laser[35] allowed us to reach a time resolution down to 30 ms, comparable to the state-of-the-art rapid-scan FTIR spectroscopy, but in a focal spot of 32 μm in the aperture-less configuration at 6 μm wavelength, not far from the diffraction limit. FTIR spectrometers can be combined with microscopes, but the smallest usable focal spot diameter rarely goes below 200 μm without compromising on the SNR, unless IR synchrotron radiation is employed as the radiation source,[36] which also allows for time-resolved experiments similar to ours.[37] Our IR microspectrometer based on a tunable QCL[33,38] can provide several other advantages over a FTIR microscope with a blackbody source: full freedom of pulse-sequence generation, high compactness with no moving parts, and high spectral resolution limited by the laser linewidth (typically 1 cm^{-1}, while most FTIR microscopes work at 8 cm^{-1} resolution, especially the more compact ones[39]). In addition to the features of the single-chip QCL model illustrated in this work, the spectral tuning range of commercial multi-chip QCL systems can reach the 5–12 μm range (850–2000 cm^{-1}), encompassing almost the entire molecular fingerprint range. It should be noted that AFM-assisted mid-IR nanospectrometers equipped with QCLs[14,23] or other mid-IR lasers[40,41] provide a much higher lateral resolution with the same spectral resolution and range as our microscope; however, they still do not have the sensitivity for time-resolved studies and, when applied to membrane proteins,[14,23] they require advanced membrane-sample preparation techniques.

Further practical advantages of our home-built QCL microscope for the study of light-sensitive proteins, if compared to large-sample area FTIR experiments, are the dramatic reduction in the total experimental time (it is no longer necessary to wait the natural dark-adaptation time before each photocycle starts) and the reduction in the quantity of membrane suspension down to a few-μl to produce mm-sized droplets instead of cm-sized films or liquid cells.

V. CONCLUSIONS

In this work, we have developed a confocal microscope for the time-resolved study of protein conformational changes with reflective objectives featuring a co-aligned, simultaneous beam path for visible light from LED sources and from a mid-infrared QCL. The LED sources are used to excite light-induced conformational changes of proteins, and the IR laser is used to probe them by vibrational spectroscopy. Triggering the XY microscope stage with the LED pulses, we can replace the area of the protein film under analysis at each LED pulse. The proteins then receive the visible illumination only once, and their photocycle always starts from the dark-adapted state. We show that this sample replacement procedure gives qualitatively different results when slow-photocycle proteins are studied, such as the slow-mutant bacteriorhodopsin D96N, widely employed for light harvesting applications.

ACKNOWLEDGMENTS

We thank Dr. Chiara Ciano for writing parts of the acquisition software. This work was partly funded by Sapienza Ricerca d'Ateneo, Sapienza University of Rome, Italy, Ministero dell'Istruzione, dell'Università e della Ricerca (MIUR) Grant No. 2017Z8TS5B, and Sapienza University of Rome Grant Nos. PH120172B3E3E36D, RM12117A5EDED70C, and AR12117A859E27F0.

AUTHOR DECLARATIONS

Conflict of Interest

The authors have no conflicts to disclose.

Author Contributions

M.E.T. and R.P. contributed equally to this work.

Maria Eleonora Temperini: Investigation (equal); Writing – original draft (equal). **Raffaella Polito**: Investigation (equal). **Antonia Intze**: Investigation (equal). **Raymond Gillibert**: Methodology (equal). **Fritz Berkmann**: Methodology (supporting). **Leonetta Baldassarre**: Investigation (equal). **Valeria Giliberti**: Investigation (equal). **Michele Ortolani**: Conceptualization (lead); Methodology (equal); Writing – original draft (equal); Writing – review & editing (lead).

26 February 2025 15:44:32

© Author(s) 2023

DATA AVAILABILITY

The data that support the findings of this study are available from the corresponding author upon reasonable request.

REFERENCES

[1]M. J. Baker, J. Trevisan, P. Bassan, R. Bhargava, H. J. Butler, K. M. Dorling, P. R. Fielden, S. W. Fogarty, N. J. Fullwood, K. A. Heys, C. Hughes, P. Lasch, P. L. Martin-Hirsch, B. Obinaju, G. D. Sockalingum, J. Sulé-Suso, R. J. Strong, M. J. Walsh, B. R. Wood, P. Gardner, and F. L. Martin, "Using Fourier transform IR spectroscopy to analyze biological materials," Nat. Protoc. **9**(8), 1771–1791 (2014).

[2]M. P. Rout and A. Sali, "Principles for integrative structural biology studies," Cell **177**(6), 1384–1403 (2019).

[3]A. Barth, "Infrared spectroscopy of proteins," Biochim. Biophys. Acta, Bioenerg. **1767**(9), 1073–1101 (2007).

[4]O. P. Ernst, D. T. Lodowski, M. Elstner, P. Hegemann, L. S. Brown, and H. Kandori, "Microbial and animal rhodopsins: Structures, functions, and molecular mechanisms," Chem. Rev. **114**(1), 126–163 (2014).

[5]Y. Jin, T. Honig, I. Ron, N. Friedman, M. Sheves, and D. Cahen, "Bacteriorhodopsin as an electronic conduction medium for biomolecular electronics," Chem. Soc. Rev. **37**(11), 2422–2432 (2008).

[6]G. Frangipane, D. Dell'Arciprete, S. Petracchini, C. Maggi, F. Saglimbeni, S. Bianchi, G. Vizsnyiczai, M. L. Bernardini, and R. Di Leonardo, "Dynamic density shaping of photokinetic *E. coli*," eLife **7**, e36608 (2018).

[7]M. Grote, M. Engelhard, and P. Hegemann, "Of ion pumps, sensors and channels—Perspectives on microbial rhodopsins between science and history," Biochim. Biophys. Acta, Bioenerg. **1837**(5), 533–545 (2014).

[8]U. K. Genick *et al.*, "Structure of a protein photocycle intermediate by millisecond time-resolved crystallography," Science **275**, 1471–1475 (1997).

[9]A. Berndt, O. Yizhar, L. A. Gunaydin, P. Hegemann, and K. Deisseroth, "Bi-stable neural state switches," Nat. Neurosci. **12**(2), 229–234 (2009).

[10]V. A. Lorenz-Fonfria, "Infrared difference spectroscopy of proteins: From bands to bonds," Chem. Rev. **120**(7), 3466–3576 (2020).

[11]J. Heberle, J. Fitter, H. J. Sass, and G. Büldt, "Bacteriorhodopsin: The functional details of a molecular machine are being resolved," Biophys. Chem. **85**(2–3), 229–248 (2000).

[12]E. R. Andresen and P. Hamm, "Site-Specific Difference 2D-IR Spectroscopy of Bacteriorhodopsin," J. Phys. Chem. B **113**(18), 6520–6527 (2009).

[13]X. Jiang, E. Zaitseva, M. Schmidt, F. Siebert, M. Engelhard, R. Schlesinger, K. Ataka, R. Vogel, and J. Heberle, "Resolving voltage-dependent structural changes of a membrane photoreceptor by surface-enhanced IR difference spectroscopy," Proc. Natl. Acad. Sci. U. S. A. **105**(34), 12113–12117 (2008).

[14]V. Giliberti, R. Polito, E. Ritter, M. Broser, P. Hegemann, L. Puskar, U. Schade, L. Zanetti-Polzi, I. Daidone, S. Corni, F. Rusconi, P. Biagioni, L. Baldassarre, and M. Ortolani, "Tip-enhanced infrared difference-nanospectroscopy of the proton pump activity of bacteriorhodopsin in single purple membrane patches," Nano Lett. **19**(5), 3104–3114 (2019).

[15]S. Mittal, K. Yeh, L. S. Leslie, S. Kenkel, A. Kajdacsy-Balla, and R. Bhargava, "Simultaneous cancer and tumor microenvironment subtyping using confocal infrared microscopy for all-digital molecular histopathology," Proc. Natl. Acad. Sci. U. S. A. **115**(25), E5651–E5660 (2018).

[16]T. Kümmel, B. van Marwick, M. Rittel, C. R. Guevara, F. Wühler, T. Teumer, B. Wängler, C. Hopf, and M. Rädle, "Rapid brain structure and tumour margin detection on whole frozen tissue sections by fast multiphotometric mid-infrared scanning," Sci. Rep. **11**(1), 11307 (2021).

[17]A. Schwaighofer, M. Brandstetter, and B. Lendl, "Quantum cascade lasers (QCLs) in biomedical spectroscopy," Chem. Soc. Rev. **46**(19), 5903–5924 (2017).

[18]M. Holz, L. A. Drachev, T. Mogi, H. Otto, A. D. Kaulen, M. P. Heyn, V. P. Skulachev, and H. G. Khorana, "Replacement of aspartic acid-96 by asparagine in bacteriorhodopsin slows both the decay of the M intermediate and the associated proton movement," Proc. Natl. Acad. Sci. U. S. A. **86**(7), 2167–2171 (1989).

[19]F. Schneider, C. Grimm, and P. Hegemann, "Biophysics of channelrhodopsin," Annu. Rev. Biophys. **44**(1), 167–186 (2015).

[20]H. A. Bechtel, M. C. Martin, T. E. May, and P. Lerch, "Improved spatial resolution for reflection mode infrared microscopy," Rev. Sci. Instrum. **80**, 126106 (2009).

[21]H. Belrhali, P. Nollert, A. Royant, C. Menzel, J. P. Rosenbusch, E. M. Landau, and E. Pebay-Peyroula, "Protein, lipid and water organization in bacteriorhodopsin crystals: A molecular view of the purple membrane at 1.9 Å resolution," Structure **7**(8), 909–917 (1999).

[22]R. Polito, M. E. Temperini, E. Ritter, L. Puskar, U. Schade, M. Broser, P. Hegemann, L. Baldassarre, M. Ortolani, and V. Giliberti, "Conformational changes of a membrane protein determined by infrared difference spectroscopy beyond the diffraction limit," Phys. Rev. Appl. **16**(1), 014048 (2021).

[23]E. Pfitzner and J. Heberle, "Infrared scattering-type scanning near-field optical microscopy of biomembranes in water," J. Phys. Chem. Lett. **11**(19), 8183–8188 (2020).

[24]D. Liberda, M. Hermes, P. Koziol, N. Stone, and T. P. Wrobel, "Translation of an esophagus histopathological FT-IR imaging model to a fast quantum cascade laser modality," J. Biophotonics **13**(8), e202000122 (2020).

[25]C. Rodig, H. Georg, F. Siebert, I. Rousso, and M. Sheves, "Temperature effects of excitation laser pulses during step-scan FT-IR measurements," Laser Chem. **19**, 169–172 (1999).

[26]V. A. Lórenz-Fonfría, V. Muders, R. Schlesinger, and J. Heberle, "Changes in the hydrogen-bonding strength of internal water molecules and cysteine residues in the conductive state of channelrhodopsin-1," J. Chem. Phys. **141**(22), 22D507 (2014).

[27]A. Intze, M. E. Temperini, L. Baldassarre, V. Giliberti, M. Ortolani, and R. Polito, "Time-resolved investigation of nanometric cell membrane patches with a mid-infrared laser microscope," Front. Photonics **4**, 1175033 (2023).

[28]K. C. Hasson, F. Gai, and P. A. Anfinrud, "The photoisomerization of retinal in bacteriorhodopsin: Experimental evidence for a three-state model," Proc. Natl. Acad. Sci. U. S. A. **93**(26), 15124–15129 (1996).

[29]R. B. Dyer, F. Gai, W. H. Woodruff, R. Gilmanshin, and R. H. Callender, "Infrared studies of fast events in protein folding," Acc. Chem. Res. **31**(11), 709–716 (1998).

[30]P. Mukherjee, I. Kass, I. T. Arkin, and M. T. Zanni, "Picosecond dynamics of a membrane protein revealed by 2D IR," Proc. Natl. Acad. Sci. U. S. A. **103**(10), 3528–3533 (2006).

[31]M. Khalil, N. Demirdöven, and A. Tokmakoff, "Coherent 2D IR spectroscopy: Molecular structure and dynamics in solution," J. Phys. Chem. A **107**(27), 5258–5279 (2003).

[32]K. Deisseroth, "Optogenetics," Nat. Methods **8**(1), 26–29 (2011).

[33]B.-J. Schultz, H. Mohrmann, V. A. Lorenz-Fonfria, and J. Heberle, "Protein dynamics observed by tunable mid-IR quantum cascade lasers across the time range from 10 ns to 1 s," Spectrochim. Acta, Part A **188**, 666–674 (2018).

[34]R. Eglof, P. Ljiljana, B. Franz, A. Emad, H. Peter, and S. Ulrich, "Time-resolved infrared spectroscopic techniques as applied to channelrhodopsin," Front. Mol. Biosci. **2**, 38 (2015).

[35]M. R. Alcaráz, A. Schwaighofer, H. Goicoechea, and B. Lendl, "EC-QCL mid-IR transmission spectroscopy for monitoring dynamic changes of protein secondary structure in aqueous solution on the example of β-aggregation in alcohol-denaturated α-chymotrypsin," Anal. Bioanal. Chem. **408**(15), 3933–3941 (2016).

[36]G. L. Carr, "Resolution limits for infrared microspectroscopy explored with synchrotron radiation," Rev. Sci. Instrum. **72**(3), 1613–1619 (2001).

[37]S. M. Rosendahl, F. Borondics, T. E. May, T. M. Pedersen, and I. J. Burgess, "Interface for time-resolved electrochemical infrared microspectroscopy using synchrotron infrared radiation," Rev. Sci. Instrum. **82**, 083105 (2011).

26 February 2025 15:44:32

© Author(s) 2023

[38]R. Maulini, A. Mohan, M. Giovannini, J. Faist, and E. Gini, "External cavity quantum-cascade laser tunable from 8.2 to 10.4 μm using a gain element with a heterogeneous cascade," Appl. Phys. Lett. **88**, 201113 (2006).
[39]A. Kenda, S. Lüttjohann, T. Sandner, M. Kraft, A. Tortschanoff, and A. Simon, "A compact and portable IR analyzer: Progress of a MOEMS FT-IR system for mid-IR sensing," Proc. SPIE **8032**, 80320O (2011).
[40]J. R. Felts, H. Cho, M.-F. Yu, L. A. Bergman, A. F. Vakakis, and W. P. King, "Atomic force microscope infrared spectroscopy on 15 nm scale polymer nanostructures," Rev. Sci. Instrum. **84**, 023709 (2013).
[41]D. Lang, J. Döring, T. Nörenberg, Á. Butykai, I. Kézsmárki, H. Schneider, S. Winnerl, M. Helm, S. C. Kehr, and L. M. Eng, "Infrared nanoscopy down to liquid helium temperatures," Rev. Sci. Instrum. **89**, 033702 (2018).

26 February 2025 15:44:32

© Author(s) 2023